Weakly Convex Discontinuity Adaptive Regularization for Microwave Imaging

Funing Bai, *Member, IEEE,* Aleksandra Pižurica, *Member, IEEE,* Ann Franchois, *Senior Member, IEEE,*
Sam Van Loocke, Daniël De Zutter, *Fellow, IEEE,* and Wilfried Philips, *Member, IEEE*

Abstract—**Reconstruction of inhomogeneous dielectric objects from microwave scattering is a nonlinear and ill-posed inverse problem. In this paper, we develop a new class of weakly convex discontinuity adaptive (WCDA) models as a regularization for quantitative microwave tomography. We show that this class includes the Huber regularizer and we show how to combine these methods with electromagnetic solvers operating on the complex permittivity profile. 2D reconstructions of objects from the Institute Fresnel database and experimental data at a single frequency demonstrate the effectiveness of the proposed regularization even when employing far less transmitters and receivers than available in the database.**

Index Terms—**Inverse problem, discontinuity adaptive regularization, microwave imaging, electromagnetic scattering.**

I. INTRODUCTION

QUANTITATIVE microwave imaging [1] forms images of internal sections of objects in a noninvasive and nondestructive way. The images are obtained by processing the scattered field data after illuminating the objects with known incident fields. Earlier regularized iterative methods to solve this nonlinear and ill-posed inverse problem include [2–10]. Total variation (TV) was applied as a multiplicative constraint in [4]. Edge preserving regularization was imposed on the real and imaginary part of the complex permittivity separately in [5]. Multiplicative Smoothing (MS) [8] tends to oversmooth the result because the smoothing is imposed all over the reconstruction domain. Value Picking (VP) [9] **is a non-spatial technique and** was shown to be effective for piecewise constant targets with several distinct permittivity values. A Markov Random Field (MRF) regularization with Line Process model was employed in [10]. Other types of MRF models, aiming at improved edge preservation and adaptation to discontinuities, so-called discontinuity-adaptive MRF models [11] have been largely studied in the domain of image processing applications, but we are not aware of any reported extensions of these models and their properties in Microwave Imaging.

In this paper, we design a new class of weakly convex discontinuity adaptive (WCDA) models as regularization functions, which satisfy the following properties: (i) can be used in convex optimization in the complex domain; (ii) discontinuity

F. Bai, A. Pižurica and W. Philips are with the Department of Telecommunications and Information Processing (IPI-TELIN-iMinds), Ghent University, St-Pietersnieuwstraat 41, B-9000 Gent, Belgium, e-mail: Funing.Bai@telin.ugent.be

A. Franchois, S. Van Loocke and D. De Zutter are with the Department of Information Technology (INTEC), Ghent University.

adaptive and (iii) with highly sensitive adaptive interaction function. We define a new method which combines these models with electromagnetic solvers in quantitative microwave tomography operating on the complex permittivity profile. Finally, we devote special attention to ensure a good sensitivity of the Adaptive Interaction Function (AIF) [11], which makes our regularization approach not only discontinuity adaptive but also sensitive to subtle changes in the underlying complex permittivity profile. Preliminary results for one special case from the proposed approach (with Huber regularization) and on simulated data only were reported in [12]. In this paper we apply the WCDA regularization to three inhomogeneous targets of the 2D Fresnel database [13] and show reconstructions obtained from single frequency data and from far less transmitters and receivers than available in the database.

This paper is organized as follows. Section II introduces the electromagnetic inverse scattering problem and Gauss-Newton optimization. The proposed method is presented in Section III and results from experimental data are shown in Section IV. Conclusions are formulated in Section V.

II. APPLICATION

Suppose an unknown object with complex permittivity $\varepsilon(\mathbf{r}) = \varepsilon'(\mathbf{r}) + i\varepsilon''(\mathbf{r})$ is embedded in free space ε_0 and is illuminated successively with different known time-harmonic incident fields (a time dependence $e^{-i\omega t}$ is assumed). In this paper we adopt a two-dimensional (2D) configuration. The discretized unknown permittivity profile $\boldsymbol{\varepsilon} = [\varepsilon_1, \cdots, \varepsilon_\nu, \cdots, \varepsilon_{N^\varepsilon}]$ is estimated iteratively, on a grid with N^ε square cells within a reconstruction domain $\mathcal{D}$, alternating between the forward and the update problem. The forward problem simulates the scattered electric field (the total field (with the object in place) minus the incident field (without the object present)) for a guessed permittivity profile, using a volume integral equation solver [14]. The scattered fields $\mathbf{e}^{scat}(\varepsilon)$ computed in a number of receiving antennas in the simulation are compared with the measured fields $\mathbf{e}^{meas}$. Based on the resulting error, the permittivity profile is updated. Typically, the inverse problem is solved by minimizing a cost function

$$F(\boldsymbol{\varepsilon}) = F^{LS}(\boldsymbol{\varepsilon}) + \mu F^D(\boldsymbol{\varepsilon}) \tag{1}$$

where $F^{LS}(\boldsymbol{\varepsilon})$ is the least squares data error and $F^D(\boldsymbol{\varepsilon})$ is a regularization term, with the parameter $\mu \geq 0$. The least squares data error is

$$F^{LS}(\boldsymbol{\varepsilon}) = \frac{\|\mathbf{e}^{meas} - \mathbf{e}^{scat}(\boldsymbol{\varepsilon})\|^2}{\|\mathbf{e}^{meas}\|^2} \tag{2}$$

where $\mathbf{e}^{meas}$ and $\mathbf{e}^{scat}(\boldsymbol{\varepsilon})$ are N^d-dimensional vectors that contain the data for all combinations of illuminating and receiving antennas.

We define the regularization function $F^D(\boldsymbol{\varepsilon})$ as

$$F^D(\boldsymbol{\varepsilon}) = \frac{1}{2} \sum_{\nu} \sum_{\nu' \in N_\nu} g_\gamma(\varepsilon_\nu - \varepsilon_{\nu'}) \quad (3)$$

where g_γ is a potential function with parameter γ and ν' denotes a spatial position neighboring ν in the neighborhood system N_ν. We use 8 neighbors in 2D as a compromise between reconstruction quality and complexity.

We consider minimization by an approximate line search along a Gauss-Newton descent direction, which requires a positive definite Hessian matrix. The complex permittivity in iteration k is updated as $\boldsymbol{\varepsilon}_{k+1} = \boldsymbol{\varepsilon}_k + \beta_k \Delta\boldsymbol{\varepsilon}_k$, where $\Delta\boldsymbol{\varepsilon}_k$ is obtained from

$$(\mathbf{J}_k^H \mathbf{J}_k + \lambda^2 \boldsymbol{\Sigma}_k^D) \Delta\boldsymbol{\varepsilon}_k = -(\mathbf{J}_k^H [\mathbf{e}^{scat}(\boldsymbol{\varepsilon}_k) - \mathbf{e}^{meas}] + \lambda^2 \boldsymbol{\Omega}_k^{D*}) \quad (4)$$

where $(.)^H$ stands for Hermitian transpose and $(.)^*$ denotes the complex conjugate, and where β_k approximately minimizes (1) along this direction [15]. The trade-off parameter λ is given by $\lambda^2 = \mu \|\mathbf{e}^{meas}\|^2$ [9]. In the following, the subscript k is omitted. $\mathbf{J}$ is the $N^d \times N^\varepsilon$ Jacobian matrix, which contains the derivatives of the scattered field components with respect to the optimization variables: $J_{d\nu} = \partial e_d^{scat}/\partial \varepsilon_\nu$; $\boldsymbol{\Omega}^{D*}$ is a N^ε-dimensional vector that contains the derivatives of the regularizing function, $\Omega_\nu^{D*} = \partial F^D/\partial \varepsilon_\nu^*$; $\boldsymbol{\Sigma}^D$ is a $N^\varepsilon \times N^\varepsilon$ matrix, $\Sigma_{\nu,\nu'}^D = \partial^2 F^D/\partial \varepsilon_{\nu'} \partial \varepsilon_\nu^*$. The use of the (independent) variables ε_ν and ε_ν^* instead of an equivalent formulation in terms of ε_ν' and ε_ν'' [16] is motivated by the more compact notations it yields for the field expressions. The factor $\mathbf{J}^H\mathbf{J} + \lambda^2 \boldsymbol{\Sigma}^D$ is known as a Gauss-Newton Hessian matrix and results from neglecting the second order derivatives $\partial^2 F/\partial \varepsilon_\nu \partial \varepsilon_{\nu'}$ and $\partial^2 F/\partial \varepsilon_\nu^* \partial \varepsilon_{\nu'}^*$ in the complex Hessian matrix [8].

III. PROPOSED WEAKLY CONVEX DISCONTINUITY ADAPTIVE CLASS OF MODELS

We design a class of regularization functions F^D in (3), that we will call weakly convex discontinuity adaptive (WCDA) models. Let η denote a complex number, being a difference between two neighboring complex permittivities: $\eta = \varepsilon_\nu - \varepsilon_{\nu'}$. The WCDA models need to satisfy the following properties:

(a) Discontinuity-adaptive, such that

$$\lim_{|\eta| \to \infty} |\frac{\partial g}{\partial |\eta|}| = \lim_{|\eta| \to \infty} |2\eta h(\eta)| = C \quad (5)$$

where $C \in [0, \infty)$ is a constant and $h(\eta)$ is the AIF. The above condition with $C = 0$ entirely prohibits smoothing at discontinuities where $|\eta| \to \infty$ whereas with $C > 0$ allows limited (bounded) smoothing. In any case, the interaction $h(\eta)$ must be small for large $|\eta|$ and approach 0 as $|\eta|$ goes to ∞.

(b) Matrix $\boldsymbol{\Sigma}^D$ is positive definite.

(c) Steep slope of AIF around the origin, to make the function sensitive to subtle changes in the permittivity profile.

The 2D Huber function

$$g_h(\eta) = \begin{cases} |\eta|^2 & |\eta| \leq \gamma \\ 2\gamma|\eta| - \gamma^2 & otherwise \end{cases} \quad (6)$$
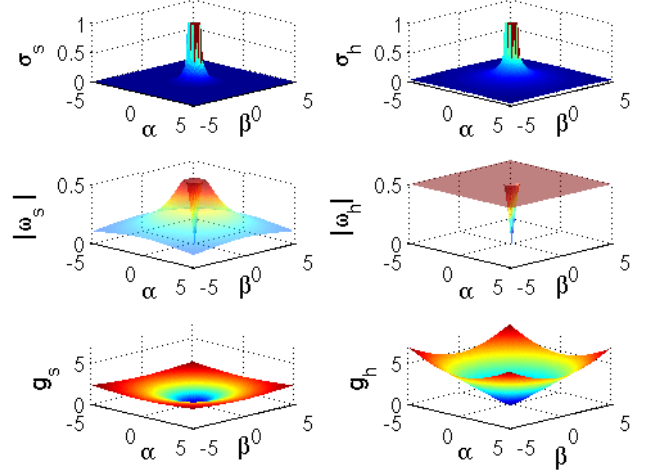

Fig. 1: The qualitative shapes of $g_s(\eta)$ and $g_h(\eta)$ from WCDA models, where $\boldsymbol{\eta} = \boldsymbol{\alpha} + \boldsymbol{\beta i}$.

satisfies these properties, so it also belongs to our class of WCDA models but with $C > 0$ (bounded smoothing). We can design similar functions with $C = 0$ (or with less smoothing of strong edges).

In particular, we can construct different discontinuity adaptive models with the desired properties by combining two well chosen functions (one in the origin and another one in the tails) like it is done in the Huber function [11]. In practice, it is convenient to start from an existing 1D discontinuity adaptive model that is convex around the origin with a steep AIF as required in (c) and replace the tails with a well-chosen function, conforming to (a)-(b). An example of such a function similar to g_h but with $C = 0$ is

$$g_s(\eta) = \begin{cases} |\eta|^2 & |\eta| \leq \gamma \\ \gamma ln(1 + \frac{|\eta|^2}{\gamma}) & otherwise \end{cases} \quad (7)$$

Note that the WCDA models and/or their first derivatives can have discontinuity points (in which case they are not strongly convex), but they conform with (b) and we show that these models (like g_s) perform well in our optimization.

Knowing that $|\eta|^2 = \eta\eta^*$, we can express $\boldsymbol{\Omega}^{D*}$ and $\boldsymbol{\Sigma}^D$ from (4) as follows

$$\Omega_\nu^{D*} = \frac{\partial F^D}{\partial \varepsilon_\nu^*} = \sum_{\nu' \in N_\nu} \omega_{\nu'}. \quad (8)$$

The diagonal elements of $\boldsymbol{\Sigma}^D$ are

$$\Sigma_{\nu,\nu}^D = \frac{\partial^2 F^D}{\partial \varepsilon_\nu \partial \varepsilon_\nu^*} = \sum_{\nu' \in N_\nu} \sigma_{\nu'} \quad (9)$$

and the non-diagonal elements are

$$\Sigma_{\nu,\nu'}^D = \frac{\partial^2 F^D}{\partial \varepsilon_{\nu'} \partial \varepsilon_\nu^*} \quad (10)$$

which are zero except if $\nu' \in N_\nu$. The expressions for $\omega_{\nu'}$, $\sigma_{\nu'}$ and $\Sigma_{\nu,\nu'}^D$ are derived in TABLE I for the g_s and g_h functions.

		$\|\varepsilon_\nu - \varepsilon_{\nu'}\| \le T_{hr}$	otherwise
$g_s(\eta)$	$\omega_{\nu'}$	$(\varepsilon_\nu - \varepsilon_{\nu'})$	$\dfrac{\gamma(\varepsilon_\nu - \varepsilon_{\nu'})}{\gamma + \|\varepsilon_\nu - \varepsilon_{\nu'}\|^2}$
$T_{hr} = \gamma$	$\sigma_{\nu'}$	1	$\dfrac{\gamma^2}{(\gamma + \|\varepsilon_\nu - \varepsilon_{\nu'}\|^2)^2}$
	$\Sigma^D_{\nu,\nu'}$	-1	$-\dfrac{\gamma^2}{(\gamma + \|\varepsilon_\nu - \varepsilon_{\nu'}\|^2)^2}$
$g_h(\eta)$	$\omega_{\nu'}$	$(\varepsilon_\nu - \varepsilon_{\nu'})$	$\dfrac{\gamma(\varepsilon_\nu - \varepsilon_{\nu'})}{\|\varepsilon_\nu - \varepsilon_{\nu'}\|}$
$T_{hr} = \gamma$	$\sigma_{\nu'}$	1	$\dfrac{\gamma}{2\|\varepsilon_\nu - \varepsilon_{\nu'}\|}$
	$\Sigma^D_{\nu,\nu'}$	-1	$-\dfrac{\gamma}{2\|\varepsilon_\nu - \varepsilon_{\nu'}\|}$

TABLE I: $\omega_{\nu'}$, $\sigma_{\nu'}$ and $\Sigma^D_{\nu,\nu'}$ for the two proposed WCDA functions.

Fig. 1 illustrates g_s and g_h in the complex domain, together with the corresponding $\|\omega\|$ and σ functions. Note that $\|\omega\|$, which is an indication of the smoothing strength, increases monotonically with $\|\eta\|$ within the "smoothing" interval (up to a threshold). Outside this interval, $\|\omega_s\|$ decreases with $\|\eta\|$ and tends to zero as $\|\eta\| \to \infty$. In other words, condition (a) with $C = 0$ entirely prohibits smoothing at discontinuities where $\|\eta\| \to \infty$ producing sharp edges. g_h with $C > 0$ allows limited (bounded) smoothing—observe that $\|\omega_h\|$ doesn't become zero when $\|\eta\| \to \infty$. The interaction σ, which performs the role of $h(\eta)$ must be small for large $\|\eta\|$ and approaches 0 as $\|\eta\|$ goes to ∞.

We optimize the regularization parameter μ and the parameter γ in the proposed model experimentally. Here $\gamma = 0.05$ is a good choice. For the regularization parameter μ we obtained the same optimal value ($\sim 1 \times 10^{-3}$) for different targets and different antenna configurations.

IV. EXPERIMENTAL VALIDATION

We consider a number of targets and antenna configurations from the 2D Fresnel database [17], for which we use TM- and TE-polarized scattered field measurements at 4GHz (λ_0 = 7.49cm). For each data set, the proposed WCDA regularization with the two potential functions (6) and (7) as well as Multiplicative Smoothing (MS) [8] and Step-wise relaxed Value Picking (SRVP) [9] regularization are employed in independent reconstructions and the results are compared. We use three quasi-lossless inhomogeneous targets: FoamDielInt, FoamDielExt and FoamTwinDiel, shown in Fig. 3 and described in [17]. The antenna positions are equally spaced on a circle with radius 1.67 m. The target is positioned in the center of this circle. For each selected transmitting antenna, the receiving antenna can be positioned on a $240°$ arc opposite to it (e.g. from $\theta_R = 60°$ to $\theta_R = 300°$ for a transmitter at $\theta_T = 0°$). We show reconstructions for which we selected 4 ($90°$ spaced) transmitting antennas (9 ($40°$ spaced) for FoamTwinDiel), each with TM and TE polarizations, and 9 ($30°$ spaced) receiving antennas, measuring the longitudinal $E_z(\theta)$ (for TM) and azimuthal $E_\theta(\theta)$ (for TE) fields, resulting in a total of 72 (162 for FoamTwinDiel) scattered fields or in a data vector $\mathbf{e}^{meas}$, containing the E_z (for TM) and E_x, E_y (for
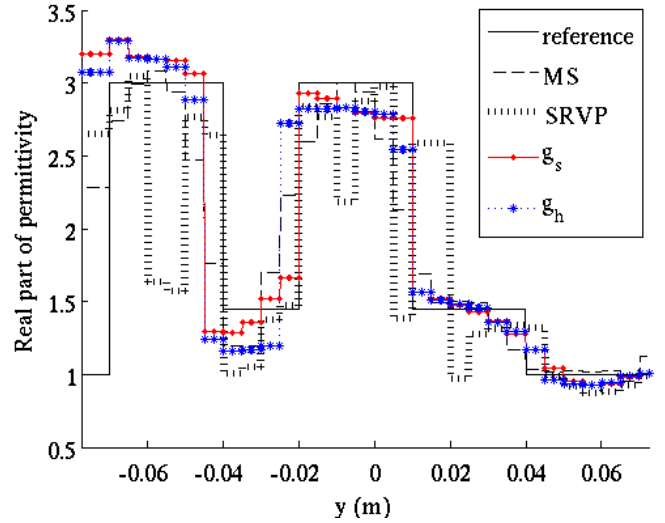

Fig. 2: Cross-sections of the reconstructed permittivity from Fig. 3 through the center of the grid for FoamTwindiel.

Reconstruction error (%)	FoamDielint	FoamDielext	FoamTwinDiel
MS	15.35	14.73	18.04
SRVP	11.13	17.00	22.09
WCDA with g_s	13.72	12.66	17.11
WCDA with g_h	13.61	13.20	17.83

TABLE II: Reconstruction error (%) for the reconstructed permittivities from Fig. 3 with the different methods.

TE) components, of length $N^d = 108$ (243 for FoamTwinDiel) complex numbers[1]. Note that the reconstructions with various methods of these targets that are reported in the special issue [13], are from *all* the transmitting positions that are available in the database: 8 transmitters (18 for FoamTwinDiel) and 241 receiving antennas, yielding data vectors up to a maximum length of 5784 (13014 for FoamTwinDiel). Smaller numbers of data may be of interest in terms of computation and measurement effort. Indeed, our reconstructions from 108 data took around 10 minutes while around 20 hours were needed when using 5784 data, with the same stopping criterion $F^{LS} = 10^{-3}$ or 20 iterations maximum, on a sixcore Intel i7 980x processor (3.33GHz) with 24GByte memory (8 threads).

All reconstructions start from a 0.15×0.15 m^2 domain $\mathcal{D}$ filled with air as an initial estimate of the permittivity (we verified experimentally that the choice of this initial estimate is not so critical by running the algorithm with several initial estimates). This domain is discretized in 30×30 square inverse problem cells (edge size = 5mm $\approx \lambda_0/15$), yielding a total of 900 permittivity unknowns. To solve the forward problem, each inverse problem cell is subdivided in $2 \times 2 = 4$ forward problem cells, which have the same permittivity. A BICGSTAB-FFT iterative solver [19] is used to accelerate the

---

[1]Note that this choice of 9 receivers appears to be close to the degrees of freedom criterion as derived in [18] and so does the number of 9 transmitters for FoamTwinDiel, eventhough we do not aim at designing experiments exactly according to this criterion. **Such comparisons are only indicative since the criterion in [18] was derived in the framework of linearized diffraction tomography (assuming a weak scatterer with a slowly spatially varying permittivity) and for non-aspect limited data.**
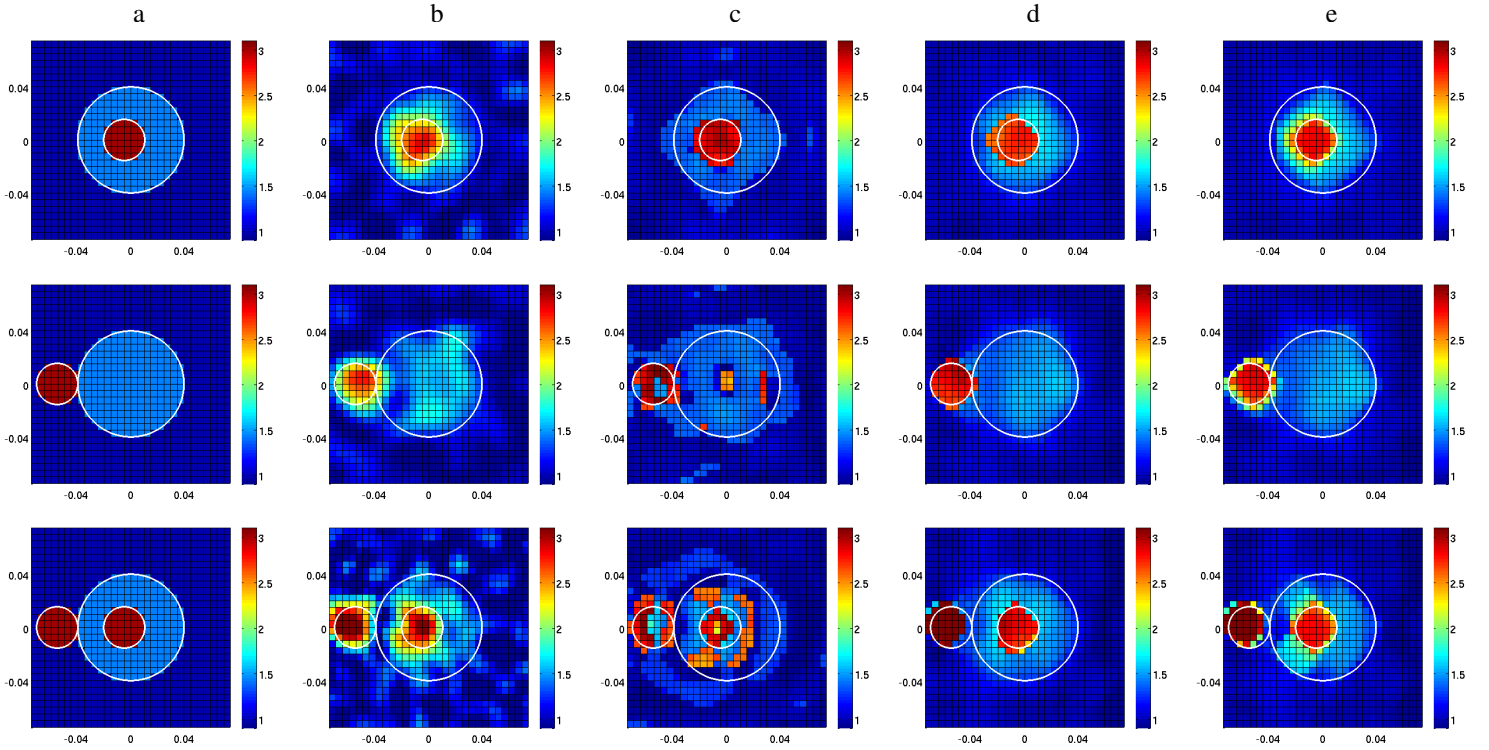
Fig. 3: Reconstruction results of different methods for three targets from the Fresnel database. Only the real parts of the permittivity profiles are shown; the imaginary parts are nearly zero. From left to right: reference (permittivities 1.45 ± 0.15 and 3 ± 0.3), MS, SRVP, WCDA with $g_s(\eta)$, WCDA with $g_h(\eta)$. From top to bottom: FoamDielInt; FoamDielExt and FoamTwinDiel.

forward solution. A calibration is applied to match amplitude and phase between measured and simulated fields: for each incidence, the measured scattered field values are multiplied with a complex factor, which is the ratio of the simulated and the measured incident fields at the receiver located opposite to the source. To evaluate the quality of the reconstructions, the reconstruction error R is defined as

$$R = \frac{\| \boldsymbol{\varepsilon}^{rec} - \boldsymbol{\varepsilon}^{ref} \|^2}{\|\boldsymbol{\varepsilon}^{ref}\|^2} \tag{11}$$

which expresses the normalized squared difference between the reconstructed $\boldsymbol{\varepsilon}^{rec}$ and the reference $\boldsymbol{\varepsilon}^{ref}$ permittivity values on the grid. The reference primittivity profiles for our experiments in Fig. 2-Fig. 4 and Table II are shown in Fig. 3.a. Fig. 3.b-e show the reconstructions with the different methods using 108 data (243 data for FoamTwinDiel). Only the real parts of the permittivities are shown, since the imaginary parts are almost zero. The regularization parameters for MS and SRVP were set as in [20]: $\mu = 2 \times 10^{-3}$ for MS and $\mu = 3$ for SRVP. The reconstructions with MS in Fig. 3.b (obtained after 20 iterations) show the plastic and—somewhat less clearly—the foam cylinders in the right locations but the images are over-smoothed as expected. The reconstructions with SRVP in Fig. 3.c yield three distinct permittivity value ranges corresponding to plastic, foam and background. FoamDielInt (at 22 iterations) is well reconstructed, although some deviations are visible in the foam contour, reflecting the use of four transmitting antennas. However, FoamDielExt (at 28 iterations) and FoamTwinDiel (at 85 iterations) show many swapped permittivity cells, as was observed also with SRVP in

[20], where 5784 (13014 for FoamTwinDiel) data were used. The reconstructions with WCDA in Fig. 3.d,e (at 20 iterations) show that the plastic cylinders are very well reconstructed in the right locations. The foam cylinders also are reconstructed in the right locations but their edges are smoother than those of the plastic cylinders—foam is less contrasting with air than plastic. Furthermore, g_s yields sharper edges than g_h while the reconstruction errors are smaller (see Table II). Overall, the WCDA results are much closer to the reference targets and this is confirmed by TABLE II and the cross-sections in Fig. 2. By comparing visually the results in Fig. 3 to the reconstructions of the same targets by a number of different methods in the special issue [13], we can conclude that WCDA yields similar or sometimes even better results from much fewer measurements. Note also that most of the results reported in [13] correspond to multifrequency measurements, while single frequency was used in our experiments. Smoothing of the foam cylinder appears to be less pronounced with the weighted L-2 norm Total Variation regularization in [21] and sharp edges of the foam cylinder are obtained with Piecewise Smoothed SRVP regularization in [20], but both of these were obtained from large data sets, and the first method used multi-frequency data (2GHz-10GHz) and a positivity enforcement while the latter method specifically is developed for piecewise (quasi-) homogeneous objects and employed an initial estimate that was closer to the solution.

In our experiments, the proposed approach yields similar improvements over the two reference methods in 3D reconstructions as well. This was illustrated for simulated
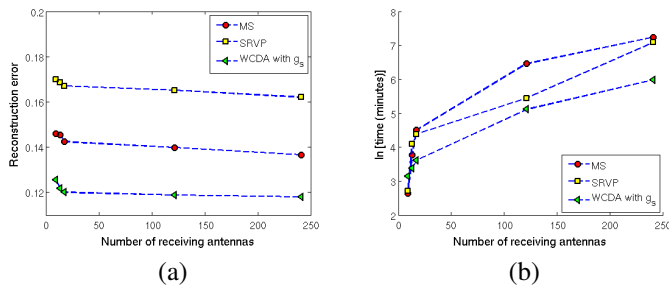
Fig. 4: Comparison between different methods in terms of (a) reconstruction error and (b) computing time as a function of the number of employed receiving antennas for FoamDielExt.

3D data in [12]. A reconstruction example obtained from experimental data from the 3D Fresnel database [22] is shown in [23]. Due to the limited space and scope of this communication, 3D reconstruction will be elaborated on in a follow-up paper.

Fig. 4 shows the reconstruction error and the reconstruction time with 8 transmitters [17] as a function of the number of receivers (9 to 241) for FoamDielExt. Clearly, the reconstruction error of the proposed method with g_s remains smallest for any number of receivers, while the computation time behaves similarly to MS. The corresponding plots for WCDA with g_h (not shown) are similar to those with g_s.

V. Conclusion

We presented a class of weakly convex discontinuity adaptive models suitable for convex optimization in the complex domain. Huber function is one of the models in this class and another function, which yields sharper edges was illustrated. When applied to electromagnetic inverse scattering, the resulting reconstructions preserve edges well and show a smaller relative error than the reference methods, even with less data points.

References

[1] M. Pastorino, *Microwave Imaging*. Hoboken, John Wiley & Sons, 2010.

[2] A. Fhager, M. Gustafsson, and S. Nordebo, "Image reconstruction in microwave tomography using a dielectric Debye model," *IEEE Trans. Biomed. Eng.*, vol. 59, no. 1, pp. 156 –166, Jan. 2012.

[3] I. Rekanos and T. Tsiboukis, "A finite element-based technique for microwave imaging of two-dimensional objects," *IEEE Trans. Instrum. Meas.*, vol. 49, no. 2, pp. 234 –239, Apr. 2000.

[4] A. Abubakar and P. Van Den Berg, "Total variation as a multiplicative constraint for solving inverse problems," *IEEE Trans. Image Process.*, vol. 10, no. 9, pp. 1384 –1392, Sept. 2001.

[5] P. Lobel, L. Blanc-Fraud, C. Pichot, and M. Barlaud, "A new regularization scheme for inverse scattering," *Inverse Problems*, vol. 13, no. 2, p. 403, 1997.

[6] P. Mojabi and J. LoVetri, "Enhancement of the Krylov subspace regularization for microwave biomedical imaging," *IEEE Trans. Med. Imaging*, vol. 28, no. 12, pp. 2015–2019, 2009.

[7] A. Golnabi, K. Paulsen, P. Meaney, and S. Geimer, "Comparison of no-prior and soft-prior regularization in biomedical microwave imaging," *J Med Phys.*, vol. 36, no. 3, pp. 159–170, 2011.

[8] J. De Zaeytijd, A. Franchois, C. Eyraud, and J.-M. Geffrin, "Full-wave three-dimensional microwave imaging with a regularized Gauss - Newton method - theory and experiment," *IEEE Trans. Antennas Propag.*, vol. 55, no. 11, pp. 3279 –3292, Nov. 2007.

[9] J. De Zaeytijd, A. Franchois, and J. Geffrin, "A new value picking regularization strategy - application to the 3-D electromagnetic inverse scattering problem," *IEEE Trans. Antennas Propag.*, vol. 57, no. 4, pp. 1133 –1149, Apr. 2009.

[10] S. Caorsi, G. Gragnani, S. Medicina, M. Pastorino, and G. Zunino, "Microwave imaging based on a Markov random field model," *IEEE Trans. Antennas Propag.*, vol. 42, pp. 293–303, Mar. 1994.

[11] S. Z. Li, *Markov Random Field Modeling in Image Analysis*, T. L. Kunii, Ed. Springer, 1995.

[12] F. Bai, A. Pižurica, S. Van Loocke, A. Franchois, D. De Zutter, and W. Philips, "Quantitative microwave tomography from sparse measurements using a robust Huber regularizer," in *IEEE Int. Conf. Image Processing (ICIP)*, Spet. 30 - Oct. 3, Orlando, Florida, USA, 2012, pp. 2073–2076.

[13] K. Belkebir and M. Saillard, "Special section on testing inversion algorithms against experimental data: inhomogeneous targets," *Inverse Problems*, vol. 21, no. 6, pp. S1–S165, 2005.

[14] S. Van den Bulcke and A. Franchois, "A full-wave 2.5D volume integral equation solver for 3D millimeter-wave scattering by large inhomogeneous 2D objects," *IEEE Trans. Antennas Propag.*, vol. 57, no. 2, pp. 535 –545, Feb. 2009.

[15] R. Fletcher, *Practical methods of optimization; (2nd ed.)*. New York, NY, USA: Wiley-Interscience, 1987.

[16] A. van den Bos, "Complex gradient and Hessian," *Proc. Inst. Elect. Eng. Vision, Image Signal Process.*, vol. 141, no. 6, pp. 380–383, 1994.

[17] J. Geffrin, P. Sabouroux, and C. Eyraud, "Free space experimental scattering database continuation: experimental set-up and measurement precision," *Inverse Problems*, vol. 21, no. 6, p. S117, 2005.

[18] A. Brancaccio, G. Leone, and R. Pierri, "Information content of born scattered fields: results in the circular cylindrical case," *J. Opt. Soc. Am. A*, vol. 15, no. 7, pp. 1909–1917, July 1998.

[19] H. A. van der Vorst, "BI-CGSTAB: a fast and smoothly converging variant of BI-CG for the solution of nonsymmetric linear systems," *SIAM J. Sci. Stat. Comput.*, vol. 13, no. 2, pp. 631–644, Mar. 1992.

[20] S. Van den Bulcke, A. Franchois, and D. De Zutter, "Piecewise smoothed value picking regularization applied to 2D TM and TE inverse scattering," *IEEE Trans. Antennas Propag.*, vol. 61, no. 6, pp. 3261–3269, June 2013.

[21] A. Abubakar, P. M. van den Berg, and T. M. Habashy, "Application of the multiplicative regularized contrast source inversion method on TM- and TE-polarized experimental Fresnel data," *Inverse Problems*, vol. 21, no. 6, pp. S5–S13, 2005.

[22] J. M. Geffrin and P. Sabouroux, "Continuing with the Fresnel database: experimental setup and improvements in 3D scattering measurements," *Inverse Problems*, vol. 25, no. 2, p. 024001, 2009.

[23] F. Bai, A. Pižurica, A. Franchois, and W. Philips, "New insights in Huber and TV-like regularizers in microwave imaging," in *IEEE Int. Conf. Image Processing (ICIP)*, Sept. 15-18, Melbourne, Australia, 2013, pp. 1026–1030.